Title

Reconstruction of carotid stenosis hemodynamics based on guidewire pressure data and computational modeling.

Permalink

Journal

Authors

Dinh, Huy
Vinuela, Fernando
Szeder, Viktor
et al.

Publication Date

DOI

Peer reviewed

Reconstruction of carotid stenosis hemodynamics based on guidewire pressure data and computational modeling

Huy Dinh, BS, **Fernando Vinuela, MD**, **Viktor Szeder, MD**, **Kasra Khatib, MD**, **Lucido Ponce Mejia, MD**, **Aichi Chien, PhD**[*]

Division of Interventional Neuroradiology, Department of Radiological Sciences, Ronald Reagan UCLA Medical Center, David Geffen UCLA School of Medicine

Abstract

Introduction—A comparative analysis between intravascular guidewire-obtained and computational fluid dynamic (CFD) flow velocity and pressure data using simplified carotid stenosis models was performed. This information was used to evaluate the viability of using guidewire pressure data to provide inlet conditions for CFD flow, and to study the relationship between stenotic length and hemodynamic behavior.

Methods—Carotid stenosis models differing in diameter and length were prepared and connected to a vascular pulsatile flow simulator. Time-dependent flow velocity and pressure measurements were taken by microcatheter guidewires and compared with CFD data.

Results—Guidewire and CFD-generated pressure profiles matched closely in all measurement locations. The guidewire was unable to reliably measure flow velocity at areas associated with higher CFD flow velocities (r = 0.92). CFD results showed that an increased length of stenosis generated expansive regions of elevated wall shear stress (WSS) within and distal to the stenosis. Low WSS was found immediately outside the stenosis outlet. An increase in stenotic length produced higher flow velocities with minimal lengthening of the distal high velocity flow jet due to faster dissipation of translational kinetic energy through turbulence.

Conclusion—We found the accuracy of guidewire-obtained velocity measurements is limited to regions unaffected by disturbed flow. WSS and turbulence behavior distal to the stenosis may be important markers to evaluate the severity of atherosclerotic progression as a function of stenotic length.

Keywords

Guidewire flow measurements; computational fluid dynamic; wall shear stress; stenosis

Introduction

Carotid atherosclerotic stenosis is one important cause of blood flow hemodynamic disturbance in the brain leading to an acute stroke [1]. It accounts for 8% to 15% of

[*]Aichi Chien, PhD, FAHA, Professor of Radiology, Physics and Biology in Medicine Graduate Program, Division of Interventional Neuroradiology, Department of Radiological Sciences, Ronald Reagan UCLA Medical Center, David Geffen School of Medicine at UCLA.

acute stroke in the population and is marked by a high rate of early recurrence, with rates up to 21% at 2 weeks and 32% at 12 weeks following the initial stroke [2, 3]. Patients with asymptomatic carotid stenosis, while at a lower risk of stroke, are at higher risk for myocardial infarction [4]. Asymptomatic carotid stenosis with more than 50% stenosis has an age-dependent prevalence in men of 0.5% to 5.7% and in women of 0.3% to 4.4%. Most patients are unaware of their condition until a stroke occurs [5, 6].

Imaging methods for characterizing carotid stenosis rely on morphology as a surrogate for hemodynamic flow. Angiography techniques such as ultrasonography, computed tomography angiography (CTA), magnetic resonance angiography (MRA) and digital subtraction angiography (DSA) are all routine clinical tools to evaluate hemodynamic influence due to stenosis [7–10]. Image-based MR flow measurements have been suggested as a way to directly measure blood flow; however, its application in stenotic vessels is limited because MRA falls short in producing high quality images in areas where the blood flow is slow and has turbulence [11–13]. Simulation calculates hemodynamic flow parameters such as velocity, pressure, wall shear stress (WSS), and overall flow behavior. Therefore, it is important because it provides consistent hemodynamic information based on fluid dynamics principles for vascular stenosis diagnostic risk assessment. Based on the presence of risks for patients to undergo surgical intervention to treat a carotid stenosis, it is desirable to obtain reliable and detailed blood flow information in the stenotic vessel area before making a therapeutic decision.

Several studies have demonstrated promising approaches for patient-specific CFD reconstruction of hemodynamics. The viability of generating robust and accurate patient-specific CFD models was demonstrated, for example, by Antiga et al.'s (2008) open source image-based framework [14]. Additional studies by De Santis et al. (2009) sought to optimize the pre-processing and mesh generation process for model construction, thereby reducing the time needed to set up a hemodynamic study without sacrificing result accuracy [15]. Other groups utilized pressure-sensing guidewires as a means of validating CFD simulation results. Fractional flow assessment via wire probing (a minimally invasive procedure) was demonstrated to be safe and feasible for *in vivo* blood pressure gradient measurements in intracranial and vertebral arterial stenosis [16–18]. Zhang et al. (2018) demonstrated the feasibility of using guidewire-based validation in their approach to CFD hemodynamic analysis of an internal carotid artery (ICA) stenosis. Their results showed good correlation between CFD simulations and pressure-wire measurements, suggesting that pressure-wire measurements themselves may serve as valid means for guiding CFD flow reconstruction [19].

In this study, we sought to perform a more thorough analysis of guidewire flow sensor technology in order to validate its applicability as a potential clinical tool for guiding CFD hemodynamic analysis of stenosis. Using simple vascular models of carotid artery stenosis, pulsatile flow velocity and pressure values were obtained using the guidewire-based and CFD reconstruction approaches. Attention was particularly directed towards the visualization of flow velocity and WSS in CFD, as these parameters are difficult to measure in clinical settings, particularly for vessels of similar or smaller sizes than the carotid arteries. In our CFD validation step, we additionally incorporated findings from other studies

that investigated hemodynamics in vascular stenosis and used those as a supplemental basis for assessing whether correct flow behavior was generated. While pressure measurements have been shown to be sufficiently accurate and reliable in many instances of both clinical research and practical use, velocity measurements have not demonstrated the same level of success. As such, we additionally analyzed the viability of guidewire flow velocity sensor usage, and critically examined its real field applicability based on performance across a range of hemodynamic environments.

Materials and Methods

Model Construction

A simplified three-dimensional model of the common carotid arteries (CCA) was used. Models were constructed in Solidworks (SW) (Dassault Systèmes SE, Vélizy-Villacoublay, France) for CFD flow measurements, and subsequently mold-casted for use in flow measurements using an intravascular guidewire. The left common carotid artery (LCCA) and right common carotid arteries (RCCA) were constructed with no difference in overall dimensions, except for the presence of a single symmetrical stenosis in the RCCA. Symmetrical stenoses of two different lengths were utilized, such that measurements could be taken and validated for two different cases of stenosis. The model configurations for the two different stenosis configurations were designated model 1 (length = 0.635 cm) and model 2 (length = 1.27 cm). Their complete dimensions are shown in Fig. 1. The dimensions of the vessel lumen diameter were chosen to be within the typical ranges for CCA lumen diameter. The dimensions of the stenosis were chosen to be within the 50–60% diameter reduction range, which is classified as a moderate-grade stenosis. Whereas a low-grade carotid stenosis (<50% stenosis) typically does not require surgery and can be treated with only medications, a high-grade stenosis (>75% stenosis) generally requires invasive treatment [20–22]. It should be noted that the decision of an invasive surgical procedure for a moderate-grade carotid stenosis is usually not easy and may be critical for future prognosis. It therefore follows that the moderate-grade stenosis is of most interest for more comprehensive risk analysis and, as such, was chosen for this study.

Guidewire Measurements

The CCA models were connected to a Left Heart Replicator flow pump (Vascular Simulations, LLC, Stony Brook, NY) that created a closed pulsating flow circuit (Fig. 2). The entire apparatus was filled with physiological saline with all air bubbles eliminated. The flow pump was equipped with electronic features that allowed adjustment of the pump force and rate. The flow pump was calibrated such that without a stenosis in the RCCA, the fluid pressure in both the RCCA and LCCA reached no higher than 120 mmHg and dropped no lower than 70 mmHg. The pump rate was set to 70 beats per minute (bpm) to model systemic flow in the body during rest conditions.

Guidewire-based measurements were performed using a Volcano ComboWire (Philips, Amsterdam, the Netherlands). The wire contains a flow sensor at its tip and a pressure sensor located 1.5 cm proximal to the tip, with a frequency range upper end estimated at approximately 1000 Hz. The wire is straight and flexible enough to allow for navigation

throughout the vascular model. Measurement readouts were displayed in real-time on the product's accompanying Volcano ComboMap screen. The wire was first calibrated in standing physiological saline outside the machine, and then guided to the appropriate measurement locations via a microcatheter.

After the set-up was allowed to run continuously for over 10 minutes, pressure and velocity measurements were recorded for at least 10 cardiac cycles at four specific locations: 2 cm proximal to the stenosis inlet, the stenosis inlet, the stenosis outlet, and 2 cm distal to the stenosis outlet. These locations were designated respectively as Vprox, Vin, Vout, and Vdist for flow velocity measurements and Pprox, Pin, Pout, and Pdist for pressure measurements. These measurements were subsequently used to validate CFD results, and for overall evaluation of guidewire usage for pressure and velocity measurements in the subsequent data analysis.

Pressure measurements were also taken further upstream at the inlet of the RCCA in order to define an inlet boundary condition for the CFD flow simulations. This time-dependent pressure boundary condition formed the key component for CFD flow reconstruction in this study. Whether or not the flow in CFD simulations that arose from this inlet boundary condition would produce a downstream flow with the expected pressure profile, velocity profile, and overall flow behavior was examined in the validation step.

CFD Measurements

RCCA stenosis models 1 and 2 were imported into SW flow simulations and meshed using an initial, uniform cartesian mesh that captured all solid walls, solid-fluid interfaces, and fluid bodies—a method which allows for mesh generation independent of the model geometry so long as its entirety remains within the computational domain [23]. The initial mesh was created to have 8 grid lengths span along vessel diameter and 6 grids lengths/cm along the path of fluid flow. Solution adaptive meshing was enabled on fluid cells such that at least 10 grids would span the length across any channel, and that the grid adequately captured changes in flow behavior around the stenosis area after the refinement process. Grid refinement also ensured that WSS was appropriately captured, particularly at the stenosis inlet and outlet where the vessel walls curve abruptly. The completed mesh contained a total of approximately 300,000 cells. Inspection of the grid refinement showed adaptive refinement was contained strictly to the stenosis area and up to 5 cm distal from the stenosis outlet, ensuring that computational resources were efficiently spent in the region of interest. Preliminary grid sensitivity analysis was performed to show correct solving and that the solution was insensitive to grid resolution at these dimensions (supplemental material). The simulation was solved at constant timesteps of 0.001 s for at least 3 cardiac cycles. An Intel Core i7-4700MQ 2.40GHz CPU, which contains 4 cores with 8 logical processors, was used for processing simulations. Computational times for simulations were between one and two hours when all cores were employed.

Fluid flow analysis was also performed using SW Flow Simulations. For the calculation, the walls of each model were given no-slip boundary conditions and treated as rigid—standardly used assumptions for CFD patient models [26,28,31,45]. Time-dependent pressure inlet profiles obtained from guidewire measurements (Fig. 3) were used to define the CFD

simulation flow inlet boundary profile, and a constant 60 mmHg pressure defined the flow outlet boundary located in the venous return compartment where flow begins to lose its pulsatility. Physiological saline was modeled in CFD as water with incompressible Newtonian fluid with density of 1000 kg/m^3 and viscosity of 0.0089 dynes/cm^2. The flow was governed by conservation of mass and momentum, which is described by the Navier-Stokes equations for incompressible flow:

$$\rho\left(\frac{\partial u}{\partial t} + u \cdot \nabla u\right) = -\nabla p + \mu \nabla^2 u + f$$

$$-\nabla \cdot u = 0$$

where u is the flow velocity, p is the pressure, t is time, ρ is the fluid density, μ is the fluid viscosity, and f is the total external force acting on the fluid. To model flow at boundary layers and predict transitions from laminar to turbulent flow, the Favre-averaged Navier-Stokes equations were used. In order to close these equations, transport equations for turbulent kinetic energy k and its dissipation rate e were employed using the k-e turbulence model proposed by Lam and Bremhorst (1981) [23]. At the flow inlet boundary, the turbulent kinetic energy k was set to 1 J/kg and the dissipation rate e was set to 1W/kg. A preliminary parameter study found that flow around the stenosis region was not significantly impacted by turbulent inlet properties.

Flow measurement techniques employed in CFD were selected for appropriate validation with wire-obtained measurements. Calculations for Vprox, Vin, Vout, and Vdist were extracted using the bulk flow velocity metric, which accounts for deviations of the flow sensor from the center of the vessel lumen and any disruptions of the velocity profile due to the presence of the microcatheter. A similar technique was employed for Pprox, Pin, Pout, and Pdist measurements, where the average cross-sectional pressure at each location was extracted. WSS, turbulence, and vorticity data were additionally obtained alongside these calculations to be used as supplemental information for examining CFD flow behavior.

Data and Statistical Analysis

Graphical velocity and pressure data from each measurement location were imported into WebPlotDigitizer where numerical data points were mapped [24]. Time-dependent graphs were generated by importing the data into Logger Pro Software (Vernier, Beaverton, OR) to perform statistical analysis, which served to identify correlations between features of the surrounding local flow environment and the degree to which wire and CFD measurements differed.

Results

Velocity

A persistent jet of increased flow velocity was observed within and distal to the stenosis in both models (Fig. 4). Flow velocities within the jet increased during systole and decreased during diastole accordingly with the normal flow found proximal to the stenosis and further

distal to the jet. The dissipation of high flow associated with the jet to within 5% of normal flow velocities occurred at 5.78 cm and 6.08 cm for models 1 and 2 respectively, as calculated from the model (Fig. 4). Higher overall flow velocities were also observed in the jet present in model 2. Both of these results arose from model 2 containing a longer segment of stenosis, which is more effective at focusing flow into a stronger jet. The jet in both models, while remaining primarily in the center of the vessel as it extends distally, was not perfectly symmetrical and fluctuated slightly in shape throughout the cardiac cycle. This asymmetry resulted from increased turbulence in the fluid flow found distal to the stenosis (Fig. 9), where propagation of inertial forces allowed the jet to wobble around the lumen axial center.

Flow separation regions containing relatively stagnant, recirculating flow were found during both systole and diastole immediately outside the jet as it exited the stenosis outlet. As stagnant flow near the wall is a well-documented phenomenon found in stenosis of many different shapes, this result is consistent with findings reported in flow studies and clinical measurements [25, 26]. Due to the symmetry of the models used in our study, a single dominant circulation on one side of the vessel wall did not develop. Furthermore, the flow separation regions did not remain stable, but periodically changed in size and shape throughout the cardiac cycle in an asymmetric fashion. From qualitative observation, occasional small bending of the high velocity jet away from a particular side of the vessel wall was associated with growth of circulations in the separation regions near that wall. The asymmetric and random fluctuation in position and size of circulations within the separation region arose due to the previously mentioned wobbling of the high velocity jet, which prevents the formation of dominant circulations regions at any fixed location.

Table 1 presents velocity measurements Vprox, Vin, Vout, and Vdist at the specified locations between CFD and wire-obtained results. Velocity measurements showed similar peak systolic values at locations proximal to the stenosis. Vprox values showed a | 2.93±19.70|% difference and a |16.65±5.28|% difference respectively for models 1 and 2. Percent differences began to increase as the measurement location was moved closer to the stenosis inlet and remained relatively high as the measurement location was moved distal to the stenosis outlet. Percent differences were most significant at the stenosis outlet for both models, with a |48.47±17.03|% difference and a |120.10±3.22|% difference respectively for models 1 and 2. Based on this trend, velocity discrepancies were generally higher at locations where CFD simulated relatively high flow velocities. Flow velocity differences were also higher in model 2 overall, as it contained the stronger high velocity jet. Quantitative analysis of the correlation between CFD simulated velocities and the measured percent difference with wire measurements showed a strong correlation (r = 0.92) between these two variables (Fig. 5). This result is consistent with the qualitative observation that differences were exacerbated most in regions of high flow velocities and minimized in regions unaffected by them.

Velocity profiles obtained from real-time monitoring of flow during guidewire measurements were compared to velocity profiles obtained from CFD analysis (Fig. 5). Guidewire measurements from both models produced velocity vs. time curves that did not intuitively follow that of the expected flow profile. Unlike the flow profiles generated via

CFD analysis, which closely followed a general shape that was nearly identical to the pressure inlet taken directly from wire measurement, the velocity profiles generated by guidewire were marked with irregular peaks and fluctuations throughout the cardiac cycle. Except in the case of model 1's Vin measurement, these wire-measured profiles consistently produced lower average velocities than observed in CFD measured profiles. Similar to the trend observed with peak systolic values, the differences were also exacerbated in regions indicated by CFD analysis to contain higher flow rates. Peaks corresponding to systole did not show up very clearly in some of these wire-obtained profiles while appearing clearly in others. CFD generated profiles for model 1 Vout and Vdist and model 2 Vdist also showed gradual downward shifting in the first two cycles. This effect may be attributed to the calculated flow solution not reaching a stable convergence criterion particularly in regions of high turbulence until the third cardiac cycle.

Pressure

Comparative fluid pressure measurements showed very close peak systolic values and minimum diastolic values between CFD calculations and guidewire obtained numerical values at all measured locations (Table 1). Peak systolic values were very close, with maximum percent differences of |3.90±0.86| % and |2.90±0.76|% respectively for models 1 and 2. Both of the highest pressure values occurred at the stenosis outlet, a phenomenon that was also observed with velocity measurements though with a larger difference in values. Comparative minimum diastolic values were also close, with maximum percent differences of |8.24±1.14|% and |5.39±1.41|% respectively for models 1 and 2. Larger overall percent differences were observed in model 1. Measurements of both peak systolic and minimum diastolic pressures obtained from CFD analysis showed continuously decreasing pressures as the measurements were moved downstream from the stenosis outlet. Wire measurements showed an overall discontinuous decrease in systolic pressure moving downstream. The systolic pressure dropped until it reached a minimum at the stenosis outlet, before rising as the pressure sensor was moved distally. Systolic pressures from both models and diastolic values from model 2 showed their lowest value at the stenosis outlet, as opposed to the measurement location furthest downstream. The pronounced dip trend in pressure recorded by the sensor at the stenosis outlet is explained by Bernoulli's principle, which predicts a localized lowering of the hydrostatic pressure in the stenosis where highest flow velocities occur. The guidewire pressure sensor, as a point measurement, appeared to be more sensitive to this effect than the CFD planar averaged measurement.

Pressure profiles obtained from real-time monitoring of flow during the wire measurement procedure were compared with pressure profiles obtained from CFD analysis (Fig. 7). At all four measurement locations, guidewire pressure sensor readings from both models produced profiles that closely follow the CFD obtained profiles. This result follows the relatively low percent differences previously measured for both peak systolic and minimum diastolic values. The slightly larger mismatches between the diastolic values than between the systolic values can also be observed in these profile comparisons, where CFD values tend to be consistently higher during diastole. Pressure differences were highest during the rapid pressure increase before the systolic peak and rapid pressure decrease after the systolic peak. Model 1's larger percent differences in diastolic values are visible, where

the wire measured pressure noticeably dropped below the CFD measured pressure. Both wire-obtained and CFD profiles demonstrated no noticeable gradual shifting up or down over time during the data sampling duration.

Wall Shear Stress

WSS contours for both models indicate that the highest WSS occurred at the stenosis inlet and the lowest occurred immediately after the stenotic outlet (Fig. 8), a result which is consistent with that produced in other models [26 – 28]. Within the stenosis, WSS peaked at the inlet and tapers off steadily towards the outlet. Peak systolic and diastolic WSS at the inlet were approximately the same between models 1 and 2, and were therefore unaffected by the stenosis length. WSS values decreased more steeply within model 2's shorter stenosis. Peak WSS values followed a time-dependent profile that closely resemble the shape of previously measured CFD time-dependent pressure and velocity profiles, where WSS peaks during systole (Fig. 8). Low WSS observed immediately after the stenosis outlet persisted throughout the entire cardiac cycle, with no notable difference in overall magnitudes across models.

Abnormal WSS also occurred in the region slightly further downstream (Fig. 8). The length affected by abnormal WSS increased with stenosis length. This region spanned approximately 0.5 – 2.5 cm from the outlet for model 1, and 0.5 – 4.5 cm from the outlet for model 2. The maximum WSS magnitudes observed in this region were considerably lower than those observed within the stenosis itself. This maximum reached an average value of 1.24 Pa and 2.60 Pa during systole for models 1 and 2 respectively, as computed by the model. WSS in this area was strongly associated with regions of increased turbulence (Fig. 8) and increased vorticity within the bulk of the flow (Fig. 10).

Turbulence

The length of the stenosis increased the magnitude and extent of turbulent kinetic energy present downstream of the stenosis (Fig. 9). In model 1, high turbulent kinetic energy persisted up to approximately 6 cm downstream from the stenosis outlet. In model 2, this length increased to approximately 8 cm. Systolic turbulence reached higher magnitudes in model 2, where maximum turbulent kinetic energies were at least 50% higher than that calculated in model 1. In both models, systolic turbulent kinetic energy profiles contained tails leading out from the stenosis wall. This dynamic phenomenon occurred because the transition from laminar to turbulent flow within the high-velocity jet propagated inward from the jet's periphery as fluid within the jet flows downstream. Elsewhere in the model, turbulence energy remained close to 0 J/kg, indicating that the flow in those regions remained mostly laminar.

Vorticity

High fluid shear stresses induced by fast flow within the stenosis introduced elevated vorticity near the walls, which subsequently propagated downstream from the stenosis outlet and was distributed to the surrounding fluid bulk (Fig. 10). Faster flow through model 2's stenosis resulted in steeper velocity gradients between the no-slip walls and the fluid bulk, thereby generating greater vorticity magnitudes and propagation extent than seen in model 1.

Vorticity was predictably higher and propagated further during systole but remained elevated throughout the cardiac cycle. Elsewhere in the model away from the region immediately downstream of the stenosis outlet, fluid rotation was minimal in the fluid bulk. Slower flow associated with normal, non-stenotic conditions upstream and further downstream from the stenosis was also marked with lower degrees fluid rotation near the vessel wall. Vorticity reached this normal state at approximately the same distances measured previously for how far high velocity flow jets extended (the distance at which flow returned to within 5% of normal velocities).

Discussion

Velocity Measurement Discrepancies and Merits

The linear regression model presented in Fig. 5 suggests that flow sensors have minimal measurement errors in vessels containing flow velocities of approximately 9.38 cm/s or under. Flow sensor measurements become less accurate as flow rates increase (Fig. 5), and it is therefore difficult to provide reliable and repeatable measurements in areas with elevated flow rates (Fig. 6). This consequently limits the utility of sensor-based collection of flow rates to the proximal region and the far distal region where the high velocity flow jet has already dissipated.

The wire, while thin and relatively flexible to facilitate maneuverability, is subject to vibrations under the pulsatile and relatively high flow velocities occurring in and downstream the stenosis. Flow pulsatility can be a significant factor that induces a lowering of the velocity threshold at which discrepancies between CFD and flow-sensor measurements become undesirable for carotid stenosis applications. Vibrations produced by the pulsatility interfere with the flow sensor data-collection, and are a probable reason flow sensor measured velocity profiles do not resemble those measured in CFD. In an environment such as the venous flow which contains less pulsatility, less wire vibrations would likely raise the velocity threshold at which flow sensor measurements would remain accurate. Thicker and more rigid wires may be able to reduce vibrations experienced in arterial flow, but at the cost of maneuverability and safe intravascular navigation.

The introduction of a wire and microcatheter into the lumen of the model creates an additional no-slip boundary not observed in the CFD simulations, in which hemodynamics are assessed without the wire's presence. This no-slip boundary introduces additional boundary layers and turbulence around the wire's measurement probe, preventing the fluid's velocity flow profile from assuming its natural form through the lumen. Flow through a cylindrical tube, such as that observed in the models away from the stenotic region, exhibits mostly laminar flow. This flow contains a radial dependence, where the highest velocities occur at the lumen center and lowest at the walls. Because technical efforts to reliably position the guidewire's measurement probe at the vessel's lumen center and away from the vessel wall may and likely will remain difficult, CFD analysis is valuable to obtain flow detailed information for stenotic vessels. [29].

Low discrepancies in regions not associated with fast flow around and immediately distal to the stenosis suggest that velocity measurements are not without merit. Vascular regions

experiencing near normal flow velocities (proximal to the stenosis inlet and over 6 cm distal to the stenosis outlet) retain good validity when using guidewire-obtained systolic velocity data. It is possible to utilize guidewire flow sensors to collect important data regarding the velocity profile further downstream to the stenotic region. For example, previous study showed that reduction in the pulsatile components of hemodynamic flow is directly related to the degree of the stenosis, and as such it could be a parameter of interest to collect via flow sensor measurements [30]. While a mismatch of time-dependent velocity profiles was observed at all measurement locations in our study (Fig. 6), this mismatch may be a potential metric used to estimate flow pulsatility, due to wire oscillations being a significant cause for disorganized, non-pulsatile velocity profiles. Wire measurements on more severely stenosed arteries with reduced pulsatility would be expected to produce less oscillations, and thus more distinguishable velocity profiles. As such, the amount of observed noise could serve as a potential indicator of hemodynamic disruption and stenosis severity.

Pressure Measurement Validity and Future Directions

Good matching between wire measurements and CFD predictions make wire usage valid for acquisition of pressure data for blood flow reconstruction. Unlike the case with velocity measurements, technical factors that make it difficult to produce repeatable velocity results are not present when measuring for pressure. Alterations to the flow profile due to the introduction of no slip boundaries on the microcatheter and wire, while affecting velocity measurements greatly, are not as significant when measuring pressure. Bernoulli's principle predicts that pressure values depend on fluid velocity and would therefore depend on the pressure sensor's radial distance from the lumen center, along with local differences in flow rates. As a point measurement, the pressure sensor varies more in this regard than the CFD calculations, likely leading to a more pronounced pressure dip recording across the stenosis. Accounting for radial differences in flow via precise positioning of the pressure sensor may be difficult, especially as the probe is moved into the narrower stenosis region. Furthermore, disturbances in fluid velocity related to induced turbulence and boundary layers from the no-slip surface of the wire and microcatheter may also contribute to this effect. While these factors make these types of pressure deviations unavoidable, they are also predictable in behavior across the two models. Similar deviations were found in other studies attempting to verify CFD results with wire probe measurements. These deviations remained minimal or consistent while the overall time-dependent pressure profiles closely overlapped one another [17, 31]. Where upstream pressure changes induced by the stenosis are ultimately more important for clinical diagnosis, these induced deviations are often found to be minimal in clinical practice. [32]

Wall Shear Stress

In this study, regions of low WSS found at the post-stenotic outlet corresponded to areas of high oscillatory shear indices (OSI) reported in other studies [26, 27]. As evident from Fig. 7, the WSS values did not increase and decrease during systole and diastole with WSS values found elsewhere along the length of the vessel. For a stenosis of approximately similar grades (50–60%), post-stenotic WSS was found to change through time with high shear indices and in a fashion completely inconsistent with the cardiac pulse to the model inlet, with values ranging between approximately 1 and −1 Pa throughout the cardiac cycle

[27]. This reported range of WSS values is in agreement with the reported systolic and diastolic WSS values at the stenosis outlet (Fig. 8). Here, high OSI along with low or no WSS have been found to be markers of post-stenotic endothelial injury and growth of the stenosis downstream by triggering plaque formation and plaque growth [33, 34, 35]. This post-stenotic region has been identified as of most importance for disease progression due to endothelial injury, plaque growth, and plaque rupture [36, 37, 38].

The region of abnormal WSS further downstream, which is accompanied by flow recirculation, high turbulence, and dispersion of vorticity into the flow bulk, is also involved in facilitating atherosclerotic growth [39]. Because of the abnormal shearing and recirculation of flow present, this region is not a healthy environment for endothelial function. The intensity and expanse of the flow recirculation region, as stressed earlier, is visibly higher in Model 2 (Fig. 4, 8, 9, 10) and therefore dependent on the length of the stenosis. Examination of Fig. 4 in conjunction with Fig. 8, 9 and 10 shows that the downstream extent of flow recirculation can be visually pinpointed to where abnormal WSS ends, where diastolic turbulence dissipates, and where systolic vorticity dissipates. Visualizations of the recirculation region in detail may be useful for clinical applications toward predicting and monitoring the extent of endothelial damage, as damage is usually not found in areas of the endothelium further downstream from the recirculation region [39].

Model Comparison

Although the use of relatively simple models may introduce biases in the interpretation of results, increasing the stenotic length introduces observable trends in downstream flow behavior that will also be present in realistic vessels. Results from Fig. 4 and Table 1 show that a doubling of the stenotic length results in an approximate 32% increase in systolic bulk velocity of the flow jet. The length of the flow jet, however, is not as noticeably affected. While a longer stenosis is more effective at accelerating flow to higher velocities, translational kinetic energy (or kinetic energy associated with linear motion of laminarly flowing fluid) within the produced jet more readily dissipates after it exits the stenosis, thereby mitigating additional velocity increases in the post-stenotic downstream flow. Fig. 9 shows that the faster dissipation of kinetic energy in model 2 translates into a more intense and extensive region of turbulent movement downstream. Because much of the increase in translational kinetic energy from a longer stenosis is ultimately converted into turbulent kinetic energy, higher turbulence induced by stenotic length increases may expose a significantly larger surface area of the post-stenotic vessel to endothelial injury, as well as subject the already compromised region to even more severely abnormal shear stresses. This is supported by the observation of a more extensive and strongly affected area of elevated WSS distal to the stenosis outlet in model 2 (Fig. 7). The affected area roughly corresponds to the zone of most intense turbulence as previously noted in Fig. 8, and as such could be a direct result of the turbulent flow inducing abnormal shearing patterns onto the vessel wall. Careful attention to the rate of turbulence-induced changes in the post-stenotic endothelium may be of high interest when assessing the disease progression between two or more stenoses of differing lengths.

Model Limitations

Our study only includes two models of a symmetric stenosis represented as perfectly cylindrical tubes with a neatly constructed narrowing. In this system, pulsating fluid flow characteristics can be treated as mostly axisymmetric with no significant persisting features on a single side of the rotational axis, allowing spatial analysis to primarily focus on hemodynamic parameter variations across the model length. While this creates an easier system to assess flow simulation results, some features that are present in a more realistic carotid stenosis are absent. Patient models are not nearly as axisymmetric, particularly at the site of stenosis even for cases classified as symmetric stenoses. Small asymmetries may play important roles in determining downstream hemodynamic behavior. For example, the equilibrium position of the post-stenotic high velocity jet and the surrounding separation zones may be easily tipped to one particular side of the vessel via small morphological asymmetries associated with the stenosis [26]. This is a feature commonly found in asymmetric stenoses, and as such additional investigation is needed to determine to what extent asymmetry or morphological deviations from our provided ideal geometry may be required to influence hemodynamic patterns. Among the biases produced due to the idealized symmetry are the observations of non-angular dependent distributions of WSS, turbulence, and vorticity downstream over time. More realistic models would likely exhibit a greater intensity of these behaviors persisting on a particular side of the vessel, such that analyses of parameters would also require an angular dependence.

Potential biases also arise from other simplifications in the model. The use of no-slip boundary conditions, while a very common simplification used in CFD studies, tends to overestimate WSS and prevent reversal of flow near the vessel walls, while the use of lower viscosity saline over blood tends to underestimate WSS. Realistic patient models also possess a small degree of vessel wall elasticity and non-Newtonian flow properties. Whether or not the presence of these factors would significantly influence simulated flow behavior is worth understanding in order to establish more conclusive relationships between the observed hemodynamic behavior and the morphologies presented in this study. In Al-Azawy (2017), it was noted that differences were found between velocity results calculated for pulsatile flow within an artificial heart. However, flow behavior in more distal arterial locations differs significantly, and the extent to which non-Newtonian velocity effects would be attenuated there is therefore far more speculative [40]. A comparative study by Al-Azawy (2020) on a simplified stenosis model, similar to the present study, investigated differences produced in a Newtonian model vs. a non-Newtonian Carreau model, and found higher vorticity and extended recirculation areas for cases of 90% arterial blockages in the Carreau model [41]. On one hand, some studies suggest that inclusion of non-Newtonian effects may produce sufficiently significant alterations to the results such that they should not be ignored, while others disagree [42]. For example, Castro et al. (2014) and Arzani (2018) provide evidence for a small impact of non-Netwonian rheology, suggesting that there is no consensus in the field at present [43–44]. Hemodynamic modeling with incorporation of non-rigid walls may also be more appropriate for evaluating tensile stresses within atherosclerotic plaques during assessment of disease progression. While the current study focuses on proof-of-concept for using guidewire-captured flow profiles for flow simulation

of simplified carotid artery models, addressing simulation properties in the future is imperative to achieve the collection of realistic hemodynamic data in patients.

The location of the stenosis in the carotid artery models in this study was sufficiently far from the end boundary such that end boundary effects could not have noticeably influenced CFD-visualized flow behavior in the region of interest. However, in the case of a model artery with a short post-stenotic length, placing the end boundary too close to the stenosis could be problematic, especially if convenient replication of an artery to a CFD model beyond a certain length to where flow begins to become non-pulsatile is not easily achievable. As the methodology is expanded to become more versatile for testing on other vessels in future studies, there will be an increasing need to develop techniques for modeling beyond the post-stenotic segment, such as the use of a diffusion compartment, so that the end boundary does not induce unwanted effects on flow within the region of interest. The need to more thoroughly model the downstream vasculature may also be useful for investigating the extent to which other factors downstream, such as the intracranial pressure, afterload, and osmotic pressure, may affect results.

Concerning the flow data collection procedure, it should be noted that while guiding the wire to the stenosis site is a minimally invasive procedure, less invasive approaches have been proposed to feed CFD carotid analysis. Xiao Li et al (2018) demonstrated the use of echocardiographic data to provide CFD flow inlet data at the common carotid artery [45]. While this method is preferable as a non-invasive procedure, the introduction of noise which reduces measurement precision remains the primary obstacle with this method [12]. In contrast, guidewire pressure measurements in the current study have shown precision and accuracy along the stenotic length to a degree not replicable by other methodologies, suggesting that guidewire measurements are not without merit. Given the trade-offs presented, a guidewire could serve as a useful alternative to echocardiogram measurements or as an additional tool to validate echocardiogram technology, and other ultrasound-based technology including Doppler velocimetry, in studying the hemodynamics of stenosis such as those in the carotid arteries.

In the stenotic vessel, assessing blood flow and wall shear stress distribution is important to evaluate the progression of stenosis. Specifically, it helps to understand how much flow is reduced by the stenosis and the likelihood of further plaque formation. In the future, utilization of the proposed analysis based on patient-specific carotid artery lumen geometry collected from clinical 3D angiographic images can be used to perform detailed analysis and collect hemodynamic data. These data could then be used to monitor whether medical therapy provides sufficient improvement to flow. They could also be used to evaluate whether an interventional procedure to implant a stent is needed to expand the stenotic region and change the hemodynamics.

Conclusion

Patient-specific hemodynamic analysis in vascular atherosclerosis would provide a diagnostic tool to analyze risk factors associated with atherosclerotic stenosis and plaque development. This study examined the possibility of using time-dependent pressure

inlet boundary conditions to guide the visualization of key flow characteristics in CFD simulations of cerebral stenosis. The utilization of guidewire pressure sensors demonstrated excellent reconstruction of parameters with promising potential for reliable data collection. In contrast, flow velocity sensor measurements were clearly affected by stenosis-induced flow jets and turbulence and demonstrated fairly limited application for hemodynamic data collection in carotid stenosis. To date, practical medical tools to measure WSS, turbulence, and vorticity parameters are not available; our study demonstrated that CFD analysis is a reasonable approach to obtain these hemodynamic data. Because WSS plays an important role in the evolution of atherosclerotic plaque, future comprehensive hemodynamic studies need to include vascular wall elasticity in the hemodynamic study to better evaluate this metric.

Supplementary Material

Refer to Web version on PubMed Central for supplementary material.

Acknowledgements

Biographies

Huy Dinh, BS in Bioengineering is currently a clinical researcher in UCLA Interventional Neuroradiology. His research interests include biomedical engineering and computational modeling.

Fernando Vinuela, MD is a Professor in UCLA Interventional Neuroradiology. He is a pioneer of endovascular therapy who led the invention of the GDC and Onix treatments. His current interest is translational research with a focus on tissue response to blood flow.

Viktor Szeder, MD, PhD. is an Associate Professor in UCLA Interventional Neuroradiology. His research focuses on improving patient outcomes using advanced endovascular techniques for acute stroke, brain aneurysms and fistulas.
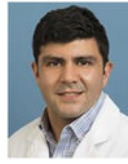
Kasra Khatibi, MD is a clinical fellow and instructor in UCLA Interventional Neuroradiology. His research interests include image guided evaluation of alteration of cerebral blood flow and brain ischemia, and endovascular treatment.

Lucido L. Ponce Mejia, MD is a clinical fellow and instructor in UCLA Interventional Neuroradiology and Diagnostic Radiology. His research interests are technology development for neuro critical care.

Aichi Chien, PhD is a Professor in UCLA Interventional Neuroradiology. Her research is to improve vascular disease treatment via translational research by integrating hemodynamic analysis, machine learning and device technology.

References

1. Yang F, Liu L, Li M, Li M, Yin Q, Guo R et al. (2013) Pattern of cerebrovascular atherosclerotic stenosis in older Chinese patients with stroke. J Clin Neurosci 20(7):979–83. 10.1016/j.jocn.2012.09.017 [PubMed: 23685106]

2. Flaherty ML, Kissela B, Sucharew H et al. (2013) The practice of carotid revascularization in a large metropolitan population. J Stroke Cerebrovasc Dis 22:143–148. 10.1016/j.jstrokecerebrovasdis.2011.07.005 [PubMed: 22056220]

3. Fairhead JF, Mehta Z, Rothwell PM (2005) Population-based study of delays in carotid imaging and surgery and the risk of recurrent stroke. Neurology 65:371–375. 10.1212/01.WNL.0000170368.82460.b4 [PubMed: 16087900]

4. Chimowitz MI, Weiss DG, Cohen SL, Starling MR, Hobson RW (1994) Cardiac prognosis of patients with carotid stenosis and no history of coronary artery disease. Veterans Affairs Cooperative Study Group 167. Stroke 25(4):759–65. 10.1161/01.STR.25.4.759 [PubMed: 8160217]

5. de Weerd M, Greving JP, Hedblad B et al. (2010) Prevalence of asymptomatic carotid artery stenosis in the general population: an individual participant data meta-analysis. Stroke 41:1294–1297. 10.1161/STROKEAHA.110.581058 [PubMed: 20431077]

6. Longstreth WT Jr, Shemanski L, Lefkowitz D et al. (1998) Asymptomatic internal carotid artery stenosis defined by ultrasound and the risk of subsequent stroke in the elderly. The Cardiovascular Health Study. Stroke 29:2371–2376. 10.1161/01.STR.29.11.2371 [PubMed: 9804651]

7. Kasner SE, Chimowitz MI, Lynn MJ, Howlett-Smith H, Stern BJ, Hertzberg VS et al. (2006) Predictors of ischemic stroke in the territory of a symptomatic intracranial arterial stenosis. Circulation 113(4):555–63. 10.1161/CIRCULATIONAHA.105.578229 [PubMed: 16432056]

8. Silvennoinen HM, Ikonen S, Soinne L, Railo M, Valanne L (2007) CT angiographic analysis of carotid artery stenosis: comparison of manual assessment, semi automatic vessel analysis, and digital subtraction angiography. AJNR Am J Neuroradiol 28(1):97–103. [PubMed: 17213433]

9. Netuka D, Belšán T, Broulíková K, Mandys V, Charvat F, Malik J et al. (2016) Detection of carotid artery stenosis using histological specimens: a comparison of CT angiography, magnetic resonance angiography, digital subtraction angiography and Doppler ultrasonography. Acta Neurochir 158(8):1505–14. 10.1007/s00701-016-2842-0 [PubMed: 27255656]

10. Loizou CP, Pattichis CS, Pantziaris M, Tyllis T, Nicolaides A (2007) Snakes based segmentation of the common carotid artery intima media. Med Biol Eng Comput 45(1):35–49. 10.1007/s11517-006-0140-3 [PubMed: 17203319]

11. Willig DS, Turski PA, Frayne R et al. (1998) Contrast-enhanced 3D MR DSA of the carotid artery bifurcation: preliminary study of comparison with unenhanced 2D and 3D time-of-flight MR angiography. Radiology 208:447–451. 10.1148/radiology.208.2.9680574 [PubMed: 9680574]

12. Jäger HR, Moore EA, Bynevelt M, Coley S, Mounfield P, Kitchen N, Taylor W (2000) Contrast-enhanced MR angiography in patients with carotid artery stenosis: comparison of two different techniques with an unenhanced 2D time-of-flight sequence. Neuroradiology 42:240–248. 10.1007/s002340050879 [PubMed: 10872166]

13. Klepaczko A, Szczypi ski P, Strzelecki M et al. (2014) Numerical modeling of MR angiography for validation of image-driven quantitative diagnosis of intracranial aneurysm and carotid stenosis. EJNMMI Phys 1, A63. 10.1186/2197-7364-1-S1-A63 [PubMed: 26501653]

14. Antiga L, Piccinelli M, Botti L et al. (2008) An image-based modeling framework for patient-specific computational hemodynamics. Med Biol Eng Comput 46: 1097. 10.1007/s11517-008-0420-1 [PubMed: 19002516]

15. De Santis G, Mortier P, De Beule M et al. (2010) Patient-specific computational fluid dynamics: structured mesh generation from coronary angiography. Med Biol Eng Comput 48: 371–380. 10.1007/s11517-010-0583-4 [PubMed: 20162466]

16. Miao Z, Liebeskind DS, Lo W et al. (2016) Fractional Flow Assessment for the Evaluation of Intracranial Atherosclerosis: A Feasibility Study. Interv Neurol 5(1–2):65–75. 10.1159/000444333 [PubMed: 27610123]

17. Han YF, Liu WH, Chen XL, Xiong YY, Yin Q, Xu GL, et al. (2016) Severity assessment of intracranial large artery stenosis by pressure gradient measurements: a feasibility study. Catheter Cardiovas Interv. 88(2):255–61. 10.1002/ccd.26414

18. Liu CP, Ling YH, Kao HL (2005) Use of a pressure-sensing wire to detect sequential pressure gradients for ipsilateral vertebral and subclavian artery stenoses. AJNR Am J Neuroradiol 26(7):1810–2. [PubMed: 16091534]

19. Zhang D, Xu P, Qiao H et al. (2018) Carotid DSA based CFD simulation in assessing the patient with asymptomatic carotid stenosis: a preliminary study. BioMed Eng OnLine 17, 31. 10.1186/s12938-018-0465-9 [PubMed: 29530025]

20. Executive Committee for the Asymptomatic Carotid Atherosclerosis Study (1995) Endarterectomy for Asymptomatic Carotid Artery Stenosis. JAMA 273:1421–28 [PubMed: 7723155]

21. Barnett HJ et al. (1998) Benefit of carotid endarterectomy in patients with symptomatic moderate or severe stenosis. North American Symptomatic Carotid Endarterectomy Trial Collaborators. N Engl J Med 339(20):1415–25. 10.1056/nejm199811123392002 [PubMed: 9811916]

22. Hobson RW 2nd et al. (2008) Society for Vascular Surgery. Management of atherosclerotic carotid artery disease: clinical practice guidelines of the Society for Vascular Surgery. J Vasc Surg 48(2):480–6. 10.1016/j.jvs.2008.05.036 [PubMed: 18644494]

23. Lam CKG, Bremhorst K (1981). A Modified Form of the k-ε Model for Predicting Wall Turbulence. ASME. J. Fluids Eng 103(3): 456–460. 10.1115/1.3240815

24. Rohatgi A, WebPlotDigitizer V4.4, Pacifica, CA. 2020 https://automeris.io/WebPlotDigitizer

25. Solzbach U, Wollschläger H, Zeiher A et al. (1987) Effect of stenotic geometry on flow behaviour across stenotic models. Med Biol Eng Comput 25:543. 10.1007/BF02441747 [PubMed: 3446976]

26. Sousa LC, Castro CF, António CC et al. (2014) Toward hemodynamic diagnosis of carotid artery stenosis based on ultrasound image data and computational modeling. Med Biol Eng Comput 52: 971–983. 10.1007/s11517-014-1197-z [PubMed: 25249277]

27. Samaee M, Tafazzoli-Shadpour M, Alavi H (2017) Coupling of shear–circumferential stress pulses investigation through stress phase angle in FSI models of stenotic artery using experimental data. Med Biol Eng Comput 55: 1147–1162. 10.1007/s11517-016-1564-z [PubMed: 27709408]

28. Zhou H, Meng L, Zhou W et al. (2017) Computational and experimental assessment of influences of hemodynamic shear stress on carotid plaque. BioMed Eng OnLine 16: 92. 10.1186/s12938-017-0386-z [PubMed: 28755660]

29. Sato H, Okamura M, Kurogane K et al. (1996) Assessment of flow velocity in saphenous vein graft using the Doppler guidewire. International Journal of Angiology 5: 24–28. 10.1007/BF02043459

30. Lee BY, Assadi C, Madden JL et al. (1978) Hemodynamics of arterial stenosis. World J. Surg 2: 621–627. 10.1007/BF01556059 [PubMed: 154211]

31. Xu P, Liu X, Zhang H et al. (2018) Assessment of boundary conditions for CFD simulation in human carotid artery. Biomech Model Mechanobiol 17: 1581–1597. 10.1007/s10237-018-1045-4 [PubMed: 29982960]

32. Fearon W, Chambers J, Seto A et al. (2017) ACIST-FFR Study (Assessment of Catheter-Based Interrogation and Standard Techniques for Fractional Flow Reserve Measurement). Circulation: Cardio Vascular Interventions 10(12): e005905. 10.1161/CIRCINTERVENTIONS.117.005905

33. Goswami P, Mandal DK, Manna NK et al. (2015) Wall Shear Stress Characteristics for the Progression of the Disease, Atherosclerosis. J Inst Eng India Ser C 96: 311–323. 10.1007/s40032-014-0161-x

34. Liu B (2007) The influences of stenosis on the downstream flow pattern in curved arteries. Medical Engineering &Physics 29(8):868–876. DOI: 10.1016/j.medengphy.2006.09.009. [PubMed: 17081795]

35. Sun N, Wood NB, Hughes AD et al. (2006) Fluid-Wall Modelling of Mass Transfer in an Axisymmetric Stenosis: Effects of Shear-Dependent Transport Properties. Ann Biomed Eng 34: 1119–1128. 10.1007/s10439-006-9144-2 [PubMed: 16791491]

36. Ojha M (1994) Wall shear stress temporal gradient and anastomotic intimal hyperplasia. Circ Res 74(6):1227–31. 10.1161/01.res.74.6.1227 [PubMed: 8187288]

37. Caro C, Fitz-Gerald J, Schroter R (1971) Atheroma and arterial wall shear observation, correlation and proposal of a shear dependent mass transfer mechanism for atherogenesis. Proc R Soc Lond B: Biol Sci 177:109–133. 10.1098/rspb.1971.0019 [PubMed: 4396262]

38. Slager C, Wentzel J, Gijsen F, Schuurbiers J, Van der Wal A, Van der Steen A, Serruys P (2005) The role of shear stress in the generation of rupture-prone vulnerable plaques. Nat Clin Pract Cardiovas Med 2: 401–407. 10.1038/ncpcardio0274

39. Cheng C, Tempel D, van Haperen R et al. (2006) Atherosclerotic Lesion Size and Vulnerability Are Determined by Patterns of Fluid Shear Stress. Circulation 113(23): 2744–2753. 10.1161/CIRCULATIONAHA.105.590018 [PubMed: 16754802]

40. Al-Azawy MG, Turan A, Revell A (2017). Investigating the impact of non-Newtonian blood models within a heart pump. Int J Numer Method Biomed Eng 33(1). doi: 10.1002/cnm.2780. Epub 2016 Apr 13.

41. Al-Azawy MG, Kadhim SK, & Hameed AS (2020). Newtonian and Non-Newtonian Blood Rheology Inside a Model of Stenosis. CFD Letters 12(11): 27–36. 10.37934/cfdl.12.11.2736

42. Saqr KM, Mansour O, Tupin S, Hassan T, Ohta M (2019) Evidence for non-Newtonian behavior of intracranial blood flow from Doppler ultrasonography measurements. Med Biol Eng Comput 57(5):1029–1036. 10.1007/s11517-018-1926-9 [PubMed: 30523533]

43. Castro Marcelo & Olivares María & Putman Christopher & Cebral Juan. (2014). Unsteady wall shear stress analysis from image-based computational fluid dynamic aneurysm models under Newtonian and Casson rheological models. Med Biol Eng Comput 52. 10.1007/s11517-014-1189-z.

44. Arzani A (2018) Accounting for residence-time in blood rheology models: do we really need non-Newtonian blood flow modeling in large arteries? J. R. Soc. Interface 15: 20180486. 10.1098/rsif.2018.0486 [PubMed: 30257924]

45. Li X, Sun B, Zhao H et al. (2018) Retrospective Study of Hemodynamic Changes Before and After Carotid Stenosis Formation by Vessel Surface Repairing. Sci Rep 8, 5493. 10.1038/s41598-018-23842-0 [PubMed: 29615730]
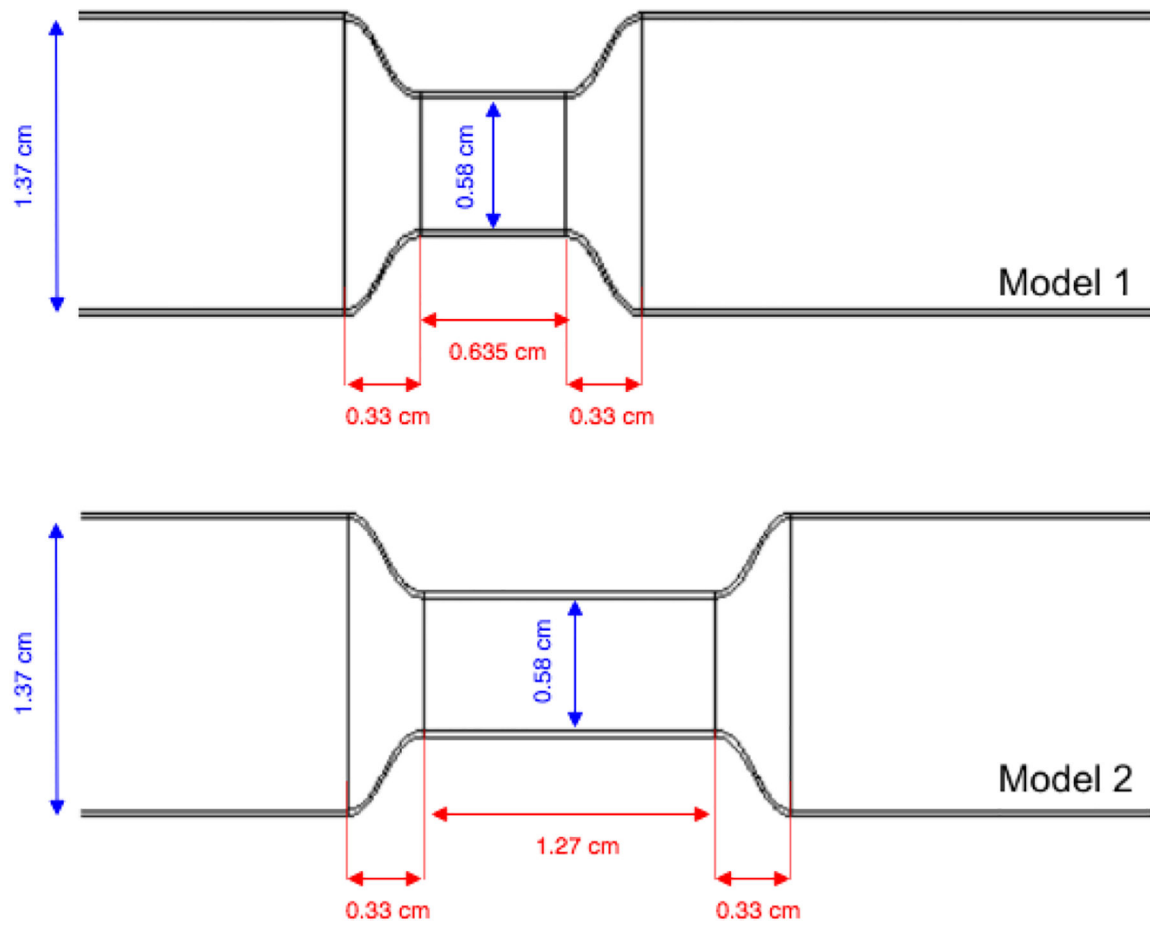
Fig. 1.
Dimensions for the stenosis regions of Models 1 and 2. Model 2 contains a stenotic region
that is twice as long as Model 1's, with all other dimensions kept the same. Models
were constructed in CFD and mold-casted with their corresponding dimensions for use in
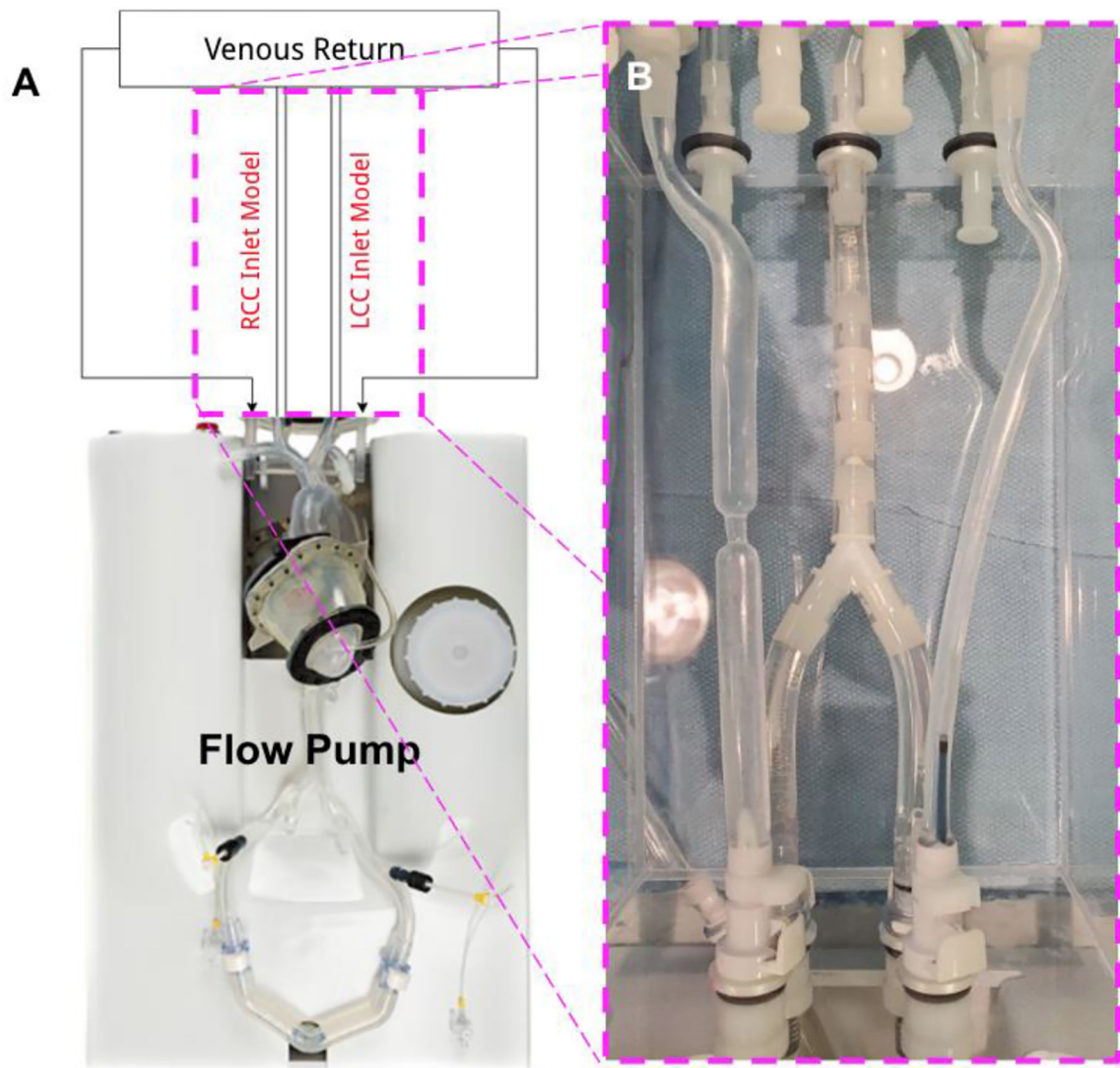guidewire flow experiments.

Fig. 2.
Flow experiment physical apparatus with flow pump attached to mold models. Flow measurements were performed by substituting Model 1 and Model 2 as the RCC artery inlet model in each respective trial. A straight, non-stenotic vessel model was kept as the LCC artery inlet model throughout the trials. Both models were connected to a flow pump and tubes that model venous return to the flow pump.
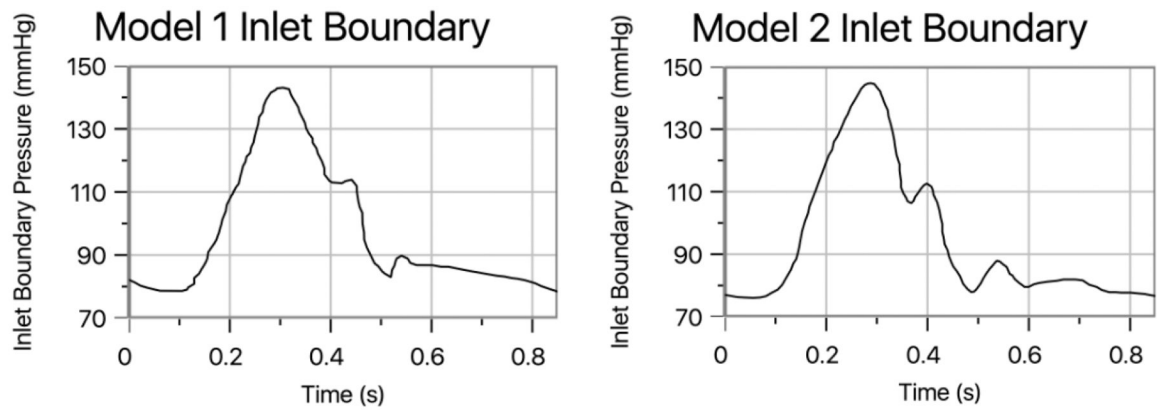
Fig. 3.
RCCA pressure profiles measured upstream of the stenosis region are used to define CFD inlet boundary conditions for model 1 (*left*) and model 2 (*right*).
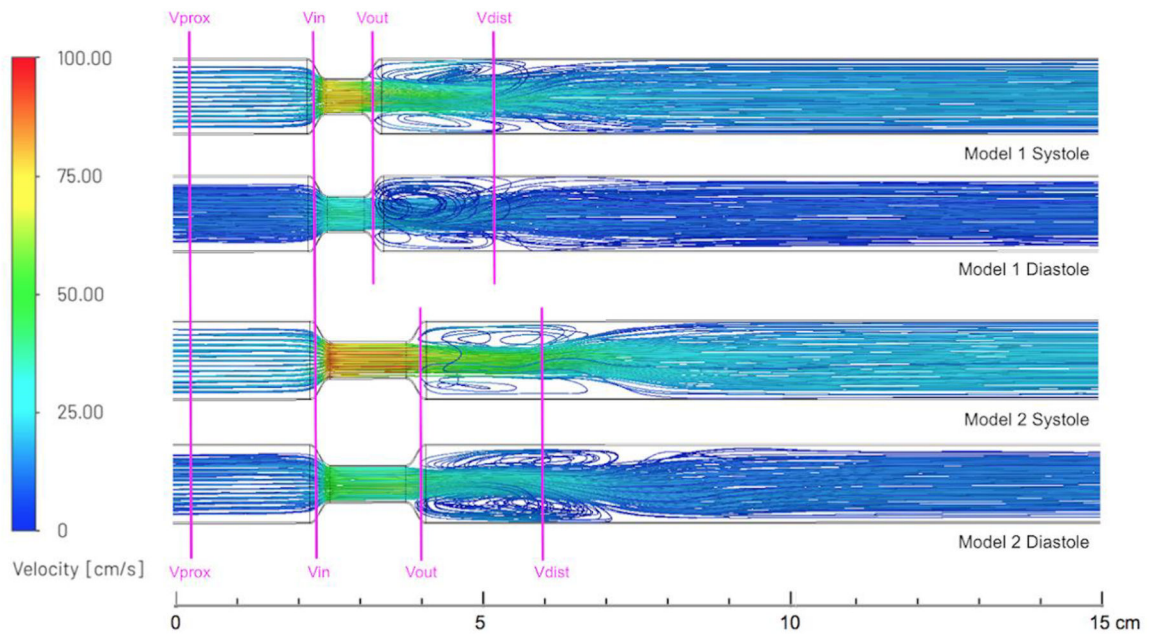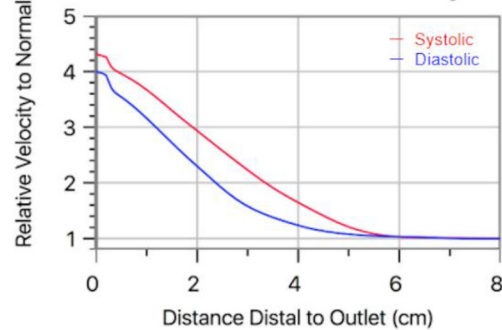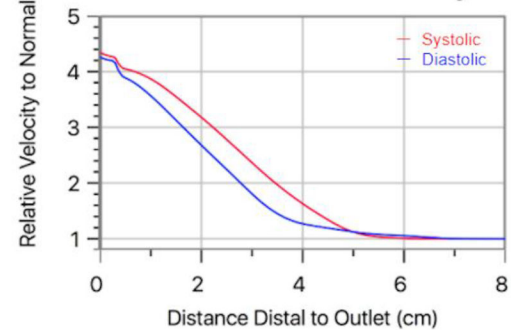
Fig. 4.
Fluid pathlines with velocity labeling by color (*top*) and graphical representation of high velocity jet extent (*bottom*) for Models 1 and 2 during systole and diastole, where relative velocity to normal refers to the ratio of measured flow velocities to baseline flow velocities not associated with stenotic flow. When stenosis length was increased, higher flow velocities were observed within the high velocity jet but the length affected by elevated flow distally experiences minimal changes. Flow lines indicate the presence of flow separation regions at the stenosis outlet, which change in shape and size throughout the cardiac cycle. Flow recirculation in the separation region consistently stretches further downstream in Model 2.
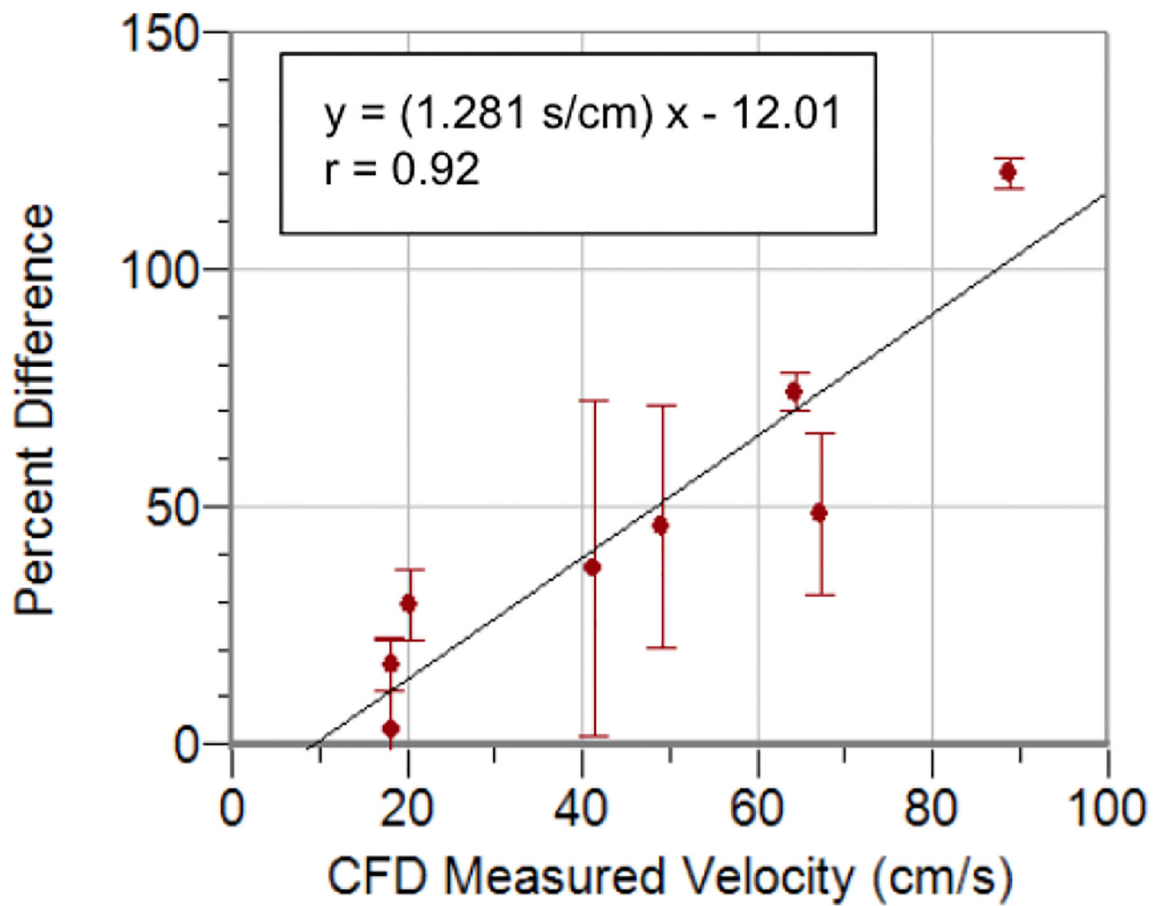
Fig. 5.
Linear regression plot of the CFD-measured velocities against percent differences from their respective wire-measured velocities using numerical data reported in Table 1. Higher discrepancies were observed as CFD measured velocities increased, suggesting that flow sensor usage for velocity measurements are most practical in environments experiencing slower flow. The model predicts minimal to no discrepancies at flow velocities of approximately 9.38 cm/s or lower.
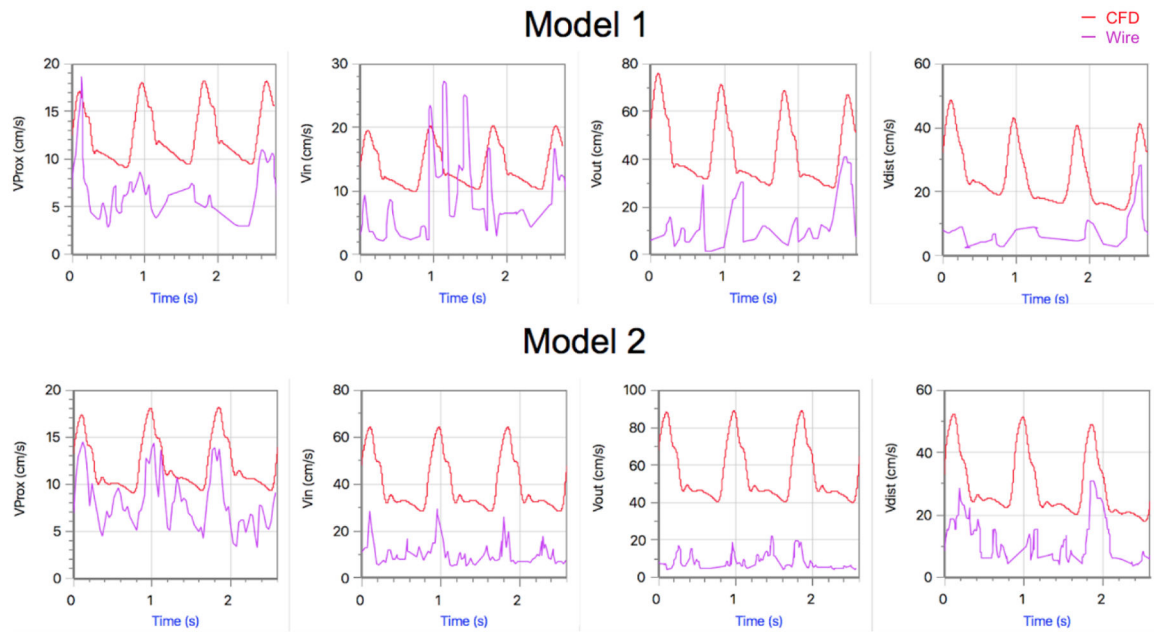
Fig. 6.
Wire vs. CFD-measured time-dependent velocity profile comparison at the specified locations in model 1 (*top*) and model 2 (*bottom*). Closest matching of profiles and systolic values were observed proximal to the stenosis, where flow velocities were expected to be the lowest. The largest mismatches were observed at the stenosis outlet, where flow velocities were expected to be the highest.
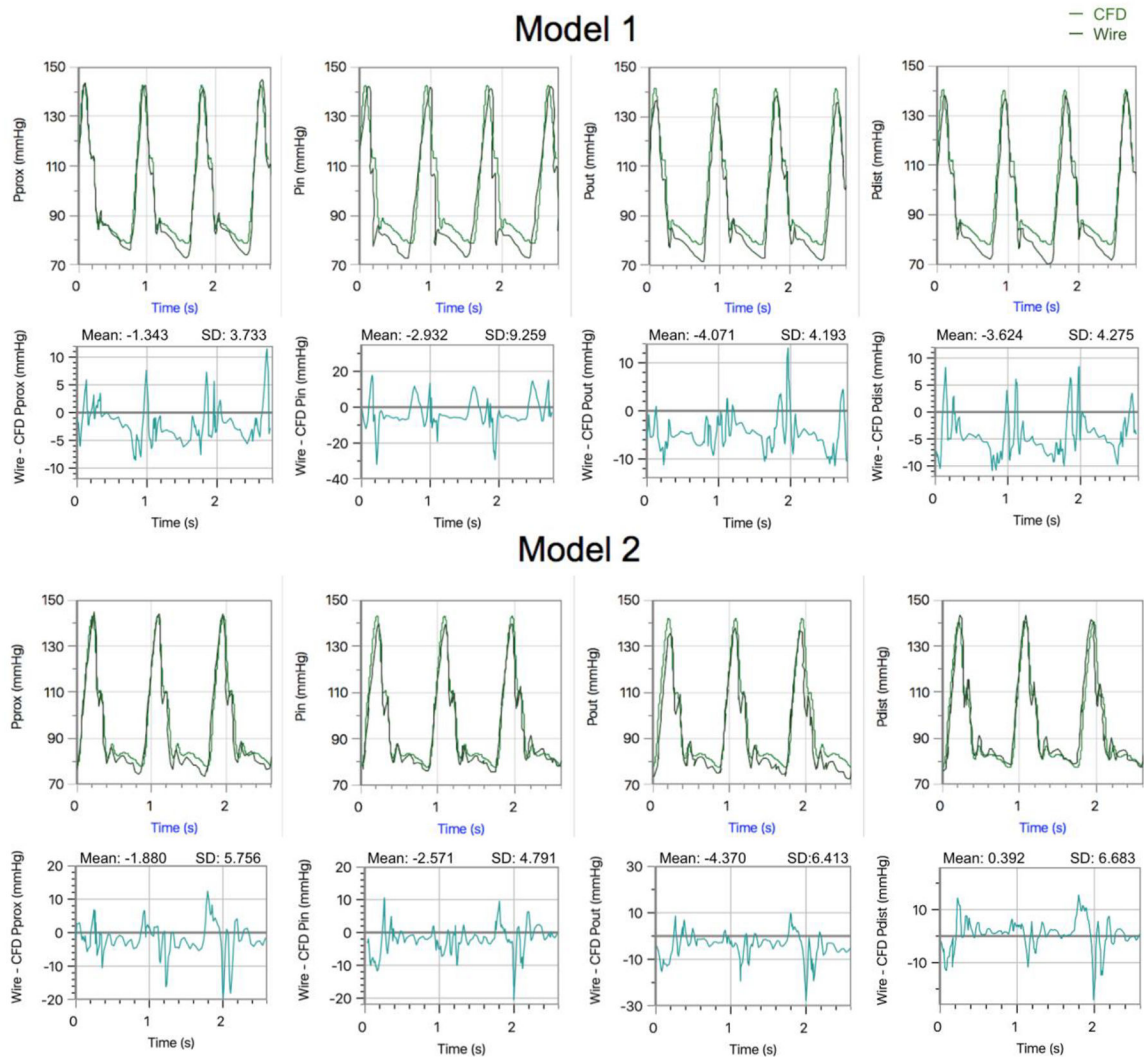
Fig. 7.
Wire vs. CFD-measured time-dependent pressure profile comparison at the specified locations in Model 1 (*top*) and Model 2 (*bottom*). Good matches were shown at all measurement locations for both models. Small mismatches were most noticeable during diastole, where wire measurements tended to record lower pressure minimums. Larger mismatches are noticeable during the fast pressure changes at the beginning and end of systole.
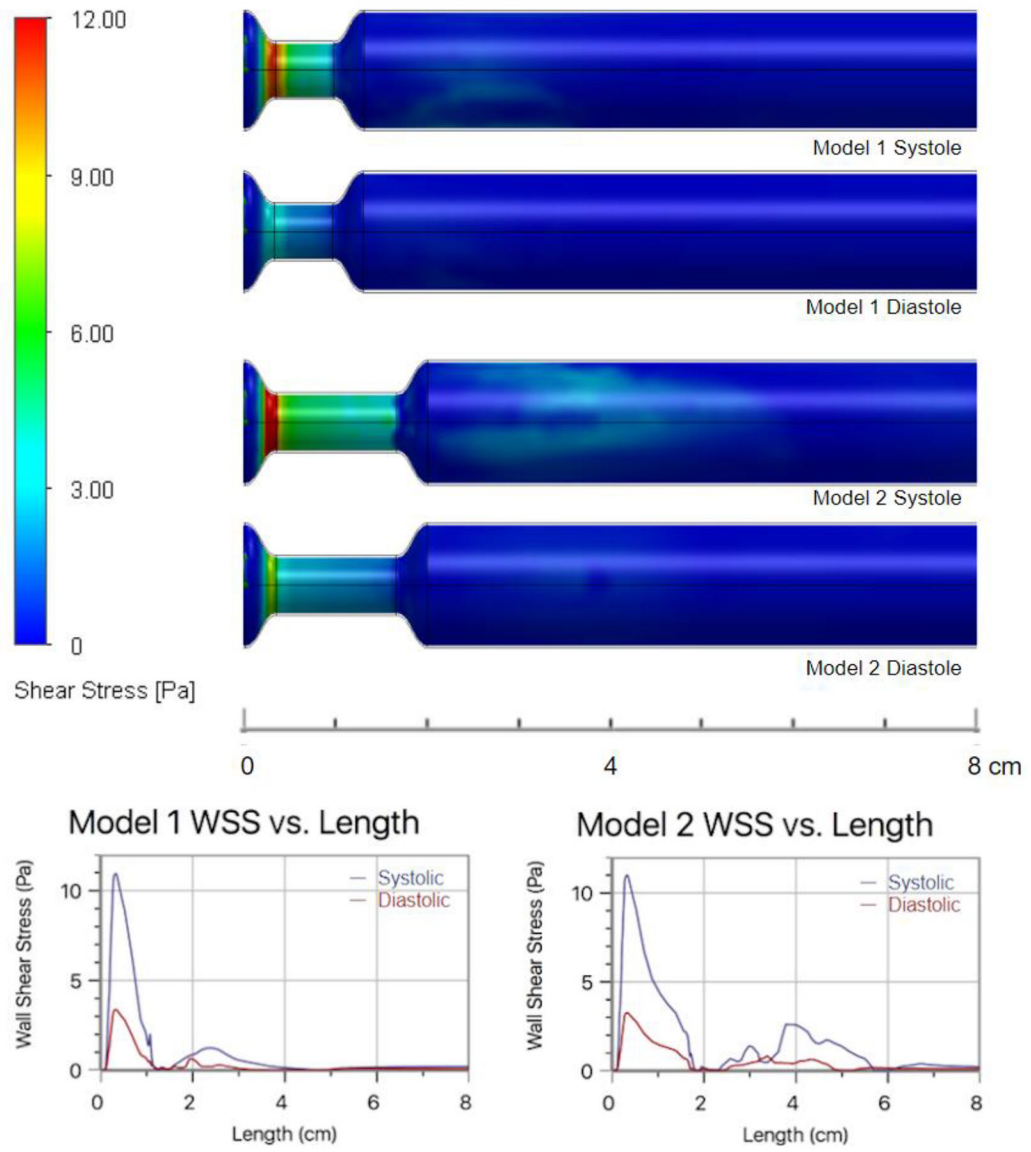
Fig. 8.
WSS contours (*top*) and corresponding graphical representation of average WSS as a function of length (*bottom*) indicated a region of very high WSS within the stenosis, a region of low and unchanging WSS at the stenosis outlet, and a region of slightly elevated WSS further downstream.
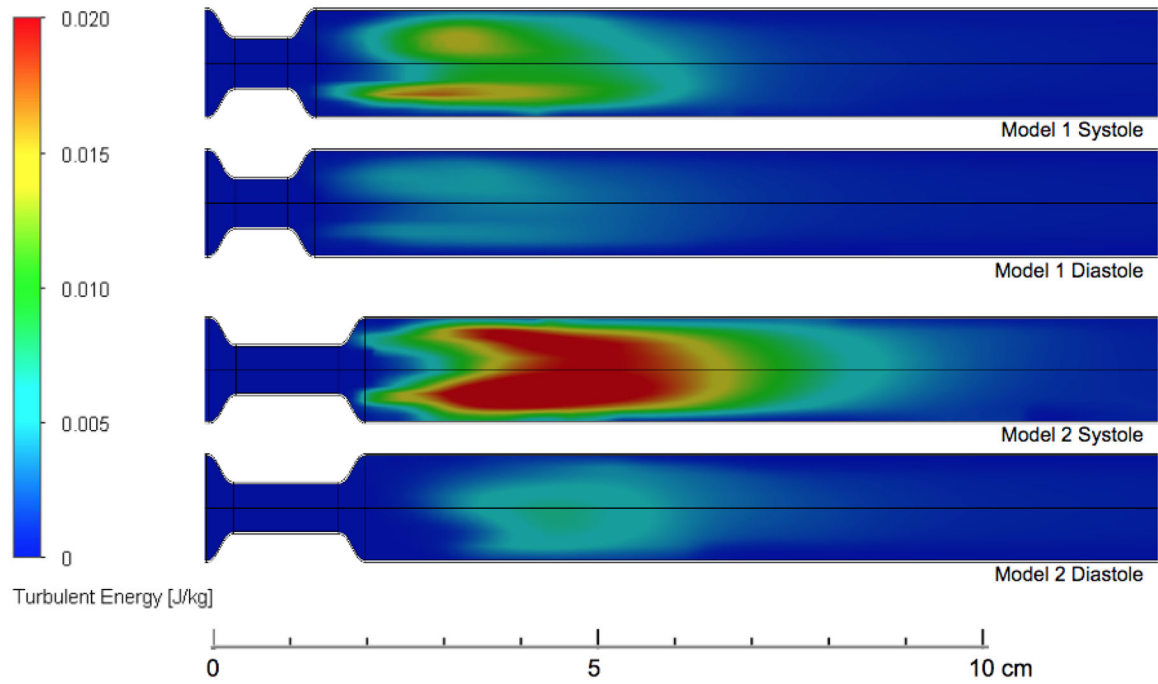
Fig. 9.
Turbulence energy contours for Models 1 and 2 during systole and diastole. Rapid conversion of translational kinetic energy into turbulent energy in Model 2 is largely responsible for reducing the higher velocities observed in the flow jet, such that flow velocities were able to return to normal levels at approximately the same distance distally in both models.
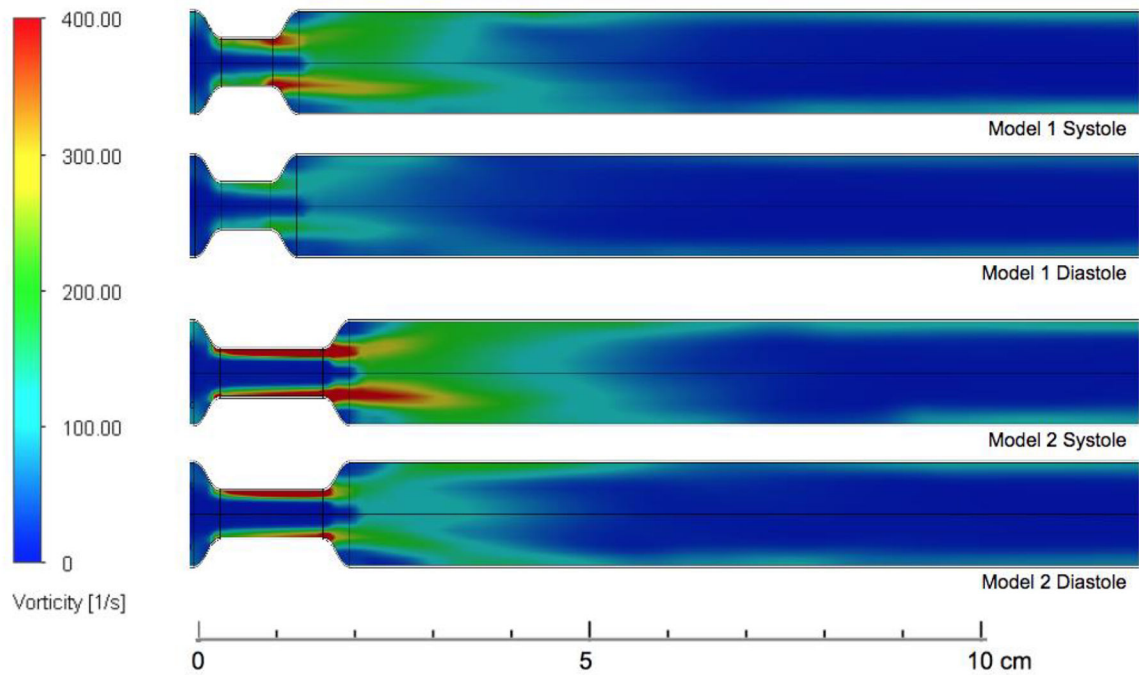
Fig. 10.
Vorticity contours for Models 1 and 2 during systole and diastole. High vorticity generated by high levels of shearing near the stenosis walls was carried downstream and propagated throughout the fluid bulk. This effect was more prominent in Model 2, which contained a faster flow jet capable of generating stronger shearing and carrying the produced vorticity downstream.

Table 1

Comparison of CFD vs. wire-obtained systolic and diastolic pressure values, and systolic velocities at the specified locations. Systolic velocities show lowest percent differences when measured proximal to the stenosis, and highest percent differences at the stenosis outlet. Diastolic velocities were not recorded, due to difficulties associated with obtaining minimum flow velocities via flow sensor. Systolic and diastolic pressure measurements showed low percent differences at all measurement locations, where slightly better matching of pressures was observed during systole

SYSTOLIC BULK FLOW VELOCITY MEASUREMENTS							
Model	Parameter	Systolic Wire Measurement (cm/s)	Systolic CFD Measurement (cm/s)	Percent Difference Systole	Diastolic Wire Measurement (cm/s)	Diastolic CFD Measurement (cm/s)	Percent Difference Diastole
1	Vprox	18.71 ± 3.72	18.17 ± 0.48	|2.93 ± 19.70| %	n/a	n/a	n/a
	Vin	27.22 ± 1.77	20.26 ± 0.30	|29.31 ± 7.53| %	n/a	n/a	n/a
	Vout	40.98 ± 5.26	67.20 ± 3.31	|48.47 ± 17.03| %	n/a	n/a	n/a
	Vdist	28.37 ± 7.54	41.31 ± 3.16	|37.14 ± 35.25| %	n/a	n/a	n/a
2	Vprox	15.40 ± 0.54	18.16 ± 0.36	|16.65 ± 5.28| %	n/a	n/a	n/a
	Vin	29.57 ± 1.34	64.28 ± 0.03	|73.97 ± 4.01| %	n/a	n/a	n/a
	Vout	22.15 ± 1.05	88.74 ± 0.22	|120.10 ± 3.22| %	n/a	n/a	n/a
	Vdist	30.79 ± 6.85	49.03 ± 1.36	|45.70 ± 25.47| %	n/a	n/a	n/a
PRESSURE MEASUREMENTS							
Model	Parameter	Systolic Wire Measurement (mmHg)	Systolic CFD Measurement (mmHg)	Percent Difference Systole	Diastolic Wire Measurement (mmHg)	Diastolic CFD Measurement (mmHg)	Percent Difference Diastole
1	Pprox	145.05 ± 1.46	142.72 ± 0.02	|1.62 ± 1.01| %	73.99 ± 1.39	78.62 ± 0.01	|6.07 ± 1.90| %
	Pin	142.31 ± 0.32	142.66 ± 0.02	|0.25 ± 0.23| %	72.96 ± 2.04	78.61 ± 0.01	|7.46 ± 2.84| %
	Pout	135.94 ± 1.14	141.35 ± 0.02	|3.90 ± 0.86| %	72.13 ± 0.72	78.22 ± 0.01	|8.10 ± 1.02| %
	Pdist	139.33 ± 0.97	140.35 ± 0.02	|0.73 ± 0.71| %	71.83 ± 0.81	78.00 ± 0.01	|8.24 ± 1.14| %
2	Pprox	145.42 ± 0.50	142.90 ± 0.02	|1.75 ± 0.36| %	73.53 ± 1.16	77.72 ± 0.01	|5.54 ± 1.60| %
	Pin	141.35 ± 0.10	143.19 ± 0.02	|1.29 ± 0.09| %	75.31 ± 1.00	77.78 ± 0.01	|3.23 ± 1.33| %
	Pout	138.00 ± 1.07	142.06 ± 0.02	|2.90 ± 0.76| %	73.50 ± 0.98	77.57 ± 0.01	|5.39 ± 1.41| %
	Pdist	143.71 ± 0.83	140.41 ± 0.02	|2.32 ± 0.71| %	75.80 ± 0.53	77.17 ± 0.01	|1.79 ± 0.72| %